Received: 31 December 2023 | Revised: 24 July 2024 | Accepted: 8 August 2024

DOI: 10.1002/jnm.3284

SPECIAL ISSUE PAPER

WILEY

Numerical modeling of HTS excited medium-speed wind generators with diode rectifier stator feeding

Robin Köster | **Andreas Binder**

Institute of Electrical Energy Conversion, Technical University Darmstadt, Darmstadt, Germany

Correspondence
Robin Köster, Institute of Electrical Energy Conversion, Technical University Darmstadt, Landgraf-Georg-Straße 4, 64287 Darmstadt, Germany.
Email: rkoester@ew.tu-darmstadt.de

Funding information
Stiftung Energieforschung Baden-Württemberg

Abstract

Medium-speed wind generators in the MW-range with high-temperature superconducting excitation winding are analyzed by means of non-linear 2D and 3D FEM models. Besides an inverter-based sinusoidal stator current feeding, a grid connection via a diode rectifier is analyzed by using coupled FEM and circuit simulations. The newly proposed modeling techniques are used to determine the excitation requirement for speed-variable, unity power factor operation at constant stator voltage, as required for a diode rectifier feeding of the stator winding. 2D FEM models in the *H*-*A*-formulation are developed and used for the calculation of the hysteresis loss in the superconducting field winding at stationary operation as well as for an investigation of field current variations in the HTS field winding. The major modeling challenges consist in very long settling times of voltage-fed models, several strong model non-linearities and high requirements on the spatial discretization. Approaches for overcoming these difficulties with reasonable computational efficiency are proposed.

KEYWORDS

coupled simulations, electrical machine, finite element simulation, high-temperature superconductor, wind generator

1 | INTRODUCTION

The increase of turbine rated power beyond $\geq 14\,\text{MW}$ and the need for alternatives to rare-earth permanent magnet (PM) generators are current trends in the wind energy sector.[1] High-temperature superconducting (HTS) field windings in electrically excited synchronous generators are a promising alternative, which has been subject of several research projects in the past decade.[2] The HTS excitation is mostly discussed in the context of gearless, direct-drive (DD) synchronous generators (rated speed $n_{\text{N}} \approx 10\,\text{rpm}$) for several advantages, such as a reduced generator mass m_{gen} and an increased generator efficiency η of conversion from mechanical to electrical power. The technological feasibility has been demonstrated in the *EcoSwing* project[3] for a gearless 3.6 MW generator. Avoiding the gear in favor of a higher reliability and a lower maintenance effort yields however very large DD generators to achieve the big generator torque. The large generator size comes along with a large amount of to date costly HTS material.

Medium-speed (MS), geared synchronous generators (rated speed $n_N = 400...600$ rpm) are more compact and avoid the failure-prone high-speed gear stage of high-speed drive trains (rated speed $n_N = 1000...1500$ rpm). The MS drive train therefore features an increasing share in off-shore wind,[4,5] which is to date still dominated by DD generators with highest rated power. Both, the reduced magnetic pole count $2p$ and the smaller generator main dimensions, that is, axial length L and stator outer diameter d_{so}, of MS generators yield a HTS material requirement, which is by more than one order of magnitude smaller than for DD generators.[6,7]

This more economical use of HTS tape allows to design the superconducting field winding in MS generators for unity power factor ($\cos\varphi_s = -1$, load sign convention) operation. This loss-free, variable DC (direct current) excitation enables alternative layouts for the connection of the generator to the collector grid: For $\cos\varphi_s = -1$, the state-of-the-art generator-side IGBT (insulated-gate bipolar transistor) rectifier can be replaced by a passive diode rectifier bridge, Figure 1. Advantages of the diode rectification consist in a higher reliability, lower costs and lower losses in the power electronics circuit. For a fixed DC link voltage, the connection via a diode rectifier bridge requires however a constant stator terminal voltage in the entire speed range $n_{min}...n_N$ of the pitch-controlled wind turbine system experiencing a broad range of wind speeds.[8] The DC generator excitation magnetomotive force (MMF) θ_f of the rotor winding must therefore be increased towards low generator speeds $n \approx n_{min}$ in order to provide a nearly constant back-EMF U_p for rectification to a constant DC link voltage. This concept therefore requires inherently a superconducting excitation winding, which is capable of providing the very high values of θ_f.

In this work, the power curve $P_{el}(n)$ of the commercially available off-shore wind turbine *Vestas V164*[9] is considered as an example. For a generator operation with unity power factor $\cos\varphi_s = -1$ at constant stator voltage U_{sN}, the proportionality $P_{el}(n) \sim I_s(n)$ holds, with $I_s(n)$ representing the torque producing, fundamental stator phase current. Figure 2 (b) visualizes the voltage and current phasor diagram of the considered generator, Section 2, at full (rated) load. The qualitative relation for the RMS phase current $I_s(n)$ versus generator speed n is shown in Figure 2 (a), together with the required air gap flux density fundamental B.

The electromagnetic modeling of the proposed HTS wind generator system, Figure 1, is challenging due to following difficulties, requiring nonstandard modeling approaches:

1. The powerful HTS excitation yields high magnetic flux densities $B \geq 4$ T in ferromagnetic active generator parts, that is, in the stator iron stack as well as in the rotor yoke and pole cores. There is a larger variation of the degree of iron saturation among different load conditions, Figure 2 (a), than in normal-conducting electrical machines. The inductances L_d, L_q feature a highly non-linear dependence on the superconducting field current I_f. The large magnetically effective air-gap width, that is, $\delta_{mag} \approx 30$ mm, Table 2, causes moreover a pronounced 2D nature of the magnetic air gap field, so that analytical models can hardly be applied.

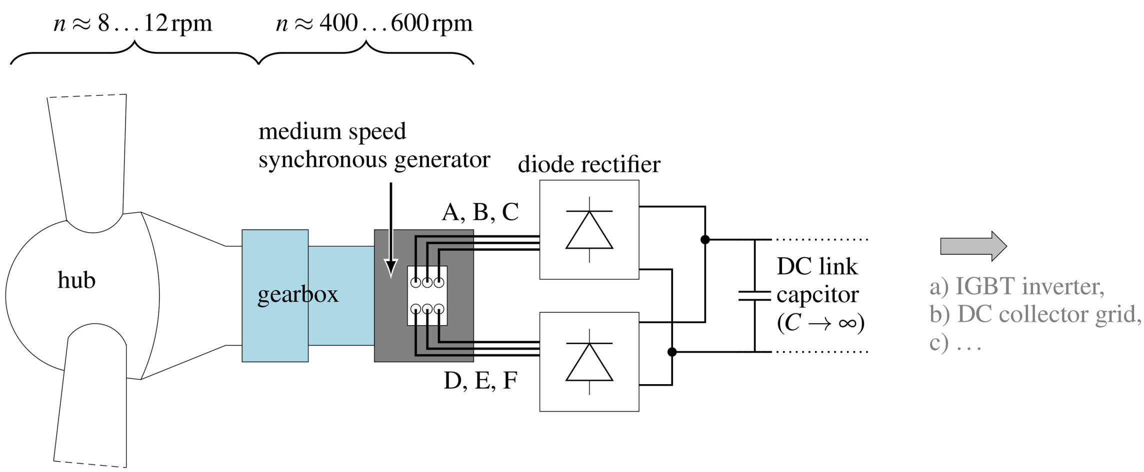

FIGURE 1 Drive train of a geared, medium-speed wind generator with a passive diode rectifier feeding of the six-phase stator winding. Several options for the connection to the collector grid exist, for example, a connection via an IGBT inverter to an AC collector grid or a direct connection to a DC collector grid. For the simulation-based analyses in this work, the limit $C \to \infty$ for the DC link capacitance is considered, that is, constant DC link voltage $U_{DCL} = \text{const.}$.

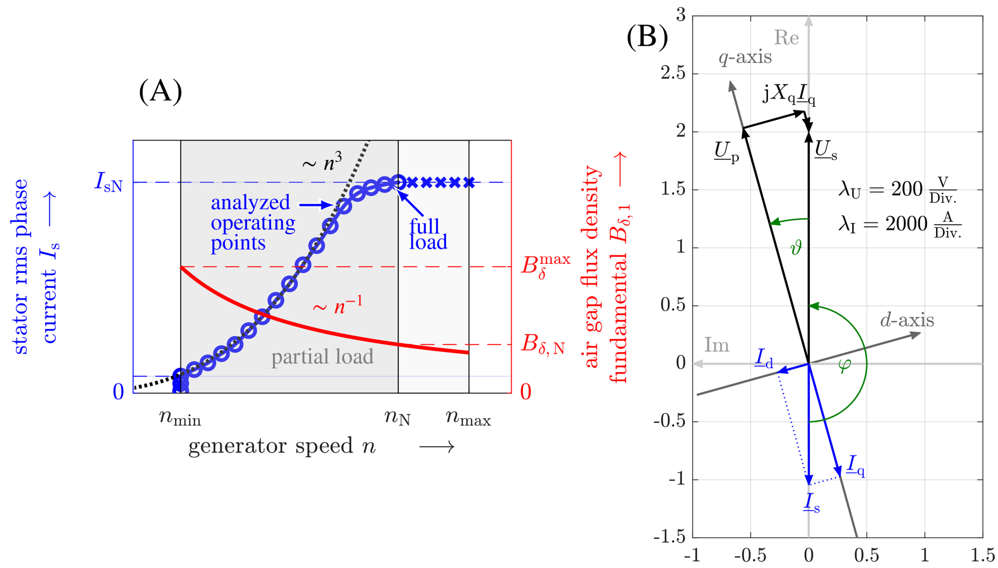

FIGURE 2 Considered operating characteristic of the HTS excited medium-speed wind generator: (A) unity power factor operation of the HTS medium-speed generator for all speeds n at fixed stator terminal voltage U_s: Stator RMS phase current I_s and approximate air gap flux density fundamental B_δ versus generator speed n. The values of $I_s(n)$ are derived from the considered power curve with the scaling $I_s(n) \sim P_{el}(n)$. ∘: Generator operating points, which are analyzed in this work, (B) phasor diagram for rated load $P_{el,N} = -5\,\mathrm{MW}$ at $\cos\varphi_s = -1$ operation, based on FE-simulation results. The very small phasors $R_s\underline{I}_s$ and $jX_d\underline{I}_d$ are omitted for better visibility.

2. The reciprocal magnetic coupling of the six stator phases, that is, the two phase-shifted three-phase systems, Figure 3, is complex and depends also on the degree of saturation in leakage flux paths. This holds particularly if the stator winding is fed with nonsinusoidal phase currents, as considered for the diode rectifier feeding, Figure 1.
3. In spite of the large inductances L_d, L_q, significant stator current harmonics are caused by the diode rectifier, so that standard current-fed finite element (FE-)models with impressed sinusoidal stator currents are not appropriate. Therefore, voltage-fed models are required, which are characterized by very long settling times until steady state conditions are reached. The high time resolution for a proper incorporation of stator current harmonics represents a contrary requirement, constituting a multi-time-scale problem.
4. 3D effects are significant and must be incorporated accurately: In contrast to current-fed FE-models, the resulting currents in voltage-fed models depend on the entire non-linear impedance per stator phase. In case of the diode rectifier feeding, the stator inductances cause a current smoothing, depending on the iron saturation state. The computationally manageable, non-linear 2D FE-models can however not cover the influence of the stator end-winding on the overall leakage inductance and on the stator phase resistance. As the considered generator, Section 2, features a rather low slimness factor L/d_{so} (L: axial generator length, d_{so}: stator outer diameter, Table 2), the relative influence of the end-winding section of the distributed stator winding is significant. An accurate modeling of the end-winding section is therefore mandatory for meaningful results for (i) the stator voltage requirement and (ii) the quantification of stator current harmonics.
5. The electrical resistance $\varrho(J)$ of the HTS winding is highly nonlinear. This prohibits the application of the standard A-formulation for electrical machines, if the superconducting winding must be explicitly modeled. Together with the non-linear $B(H)$-relation of the ferromagnetic generator parts, this constitutes the need for coupled formulations, Section 5.
6. The small dimensions of the HTS conductors require a very fine spatial resolution to get meaningful results for the superconducting current distribution in the field winding and for the hysteresis losses. In contrast, the generator dimensions are by several orders of magnitude larger, constituting also a multi-length-scale problem. The trade-off between sufficient local, spatial resolution and computational efficiency for the full-size generator model is aggravated by the multi-time-scale nature mentioned in Section 3.
7. In contrast to most discussed HTS generator concepts, the unity power factor ($\cos\varphi_s = -1$) at fixed stator voltage U_{sN} requires a continuous variation of the superconducting field current I_f. The model must therefore enable a

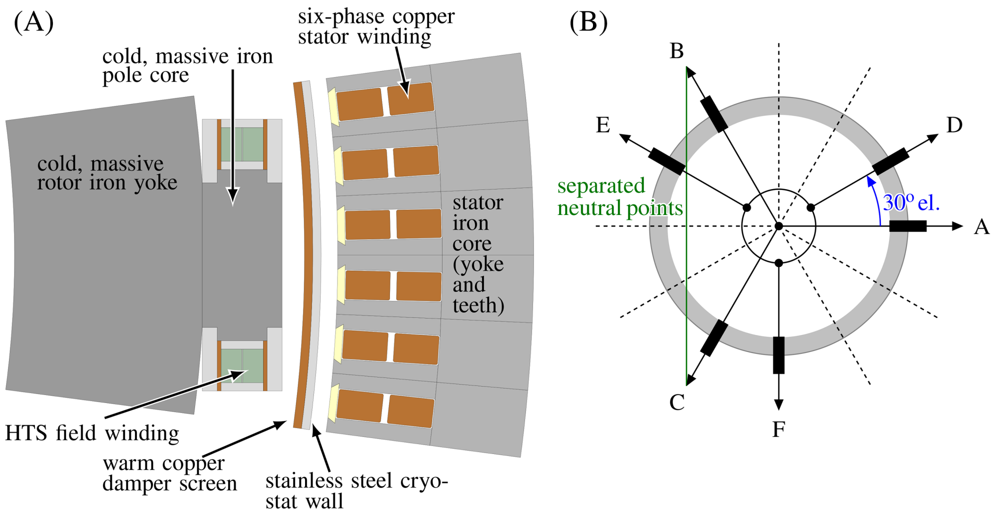

FIGURE 3 (A) One pole of the HTS excited medium-speed wind generator. The vacuum chamber rotates and encloses the entire rotor. The copper damper screens the cold rotor parts from asynchronously rotating air gap magnetic field harmonics. The short-pitched, two-layer, six-phase stator winding with one slot per pole and phase lies in open slots. (B) Schematic of the six-phase winding: The 3-phase subsystems A, B, C and D, E, F feature a phase shift of 30° el. Green line (—): With separate neutral points, the available line-to-line voltage is the same as for a single three-phase winding.

determination of (i) the hysteresis losses $P_{\mathrm{d,hyst}}$ in the HTS field winding and (ii) the voltage requirement u_{f} in the field circuit.

This work proposes a modeling framework, which allows to deal with these challenges by using several FE-models. Details of the generator concept are summarized in Section 2. The general modeling method and the implemented work flow are described in Section 3. Section 4 is on the coupling of the diode rectifier circuit and 2D non-linear FE-models. Surface coupled 2D models in the *H-A*-formulation are used in Section 5 for the characterization of the HTS field winding. Here, the hysteresis loss calculation at stationary conditions and for field current variations serve as examples, before the results are summarized in Section 6.

2 | SIX-PHASE HTS GENERATOR CONCEPT

The 5 MW, 500 rpm MS synchronous generator, Table 1, features an all-iron topology with ferromagnetic rotor structure, that is, yoke and pole cores made from FeNi9 (9% nickel steel), and a stator back iron, Figure 3 (a), to guide the magnetic flux with low reluctance. The six-phase, distributed stator copper winding lies in open stator slots. This topology minimizes the rotor excitation requirement and, hence, the amount of costly HTS material. The cold, massive rotor iron parts are made from FeNi9,[10] while the warm stator core is made from steel laminations M470-65A.[11] The copper damper screen is attached to the inner side of the stainless steel cryostat wall in order to decrease the eddy current loss caused by air gap field pulsations due to stator slot openings. An iterative design procedure is applied to design the HTS field winding, Section 3. The key characteristics of the generator are listed in Table 1.

The six-phase stator winding comprises two 3-phase subsystems, that is, A, B, C and D, E, F, with a phase shift of 30° el., Figure 3 (b). Compared to a three-phase winding, it enables a higher fundamental winding factor. As the two subsystems feature separate neutral points to avoid additional current harmonics if connected in parallel, the line-to-line voltage is $U_{\mathrm{LL}} \approx 1.73 \cdot U_{\mathrm{s}}$ with U_{s} as RMS stator fundamental phase voltage.

The low-voltage stator winding is connected to the diode rectifiers, Figure 4, and a constant DC link voltage (1) is impressed.

$$U_{\mathrm{DCL}} = \frac{3 \cdot \sqrt{2}}{\pi} \cdot U_{\mathrm{LL}} \approx 932\,\mathrm{V} \tag{1}$$

TABLE 1 Main characteristics of the six-phase, HTS excited medium-speed wind generators for diode rectifier feeding. The phasor diagram for rated operation is shown in Figure 2 b).

Rated electrical output power	$P_{\mathrm{el,N}}$	-5 MW
Rated generator speed	n_{N}	500 rpm
Minimum generator speed	$n_{\min}$	192 rpm
Rated stator voltage	U_{N}	690 V
Rated stator current	I_{sN}	2092 A
Rated power factor	$\cos\varphi_{\mathrm{s}}$	-1
Pole count	$2p$	24
Rated stator frequency	f_{sN}	100 Hz

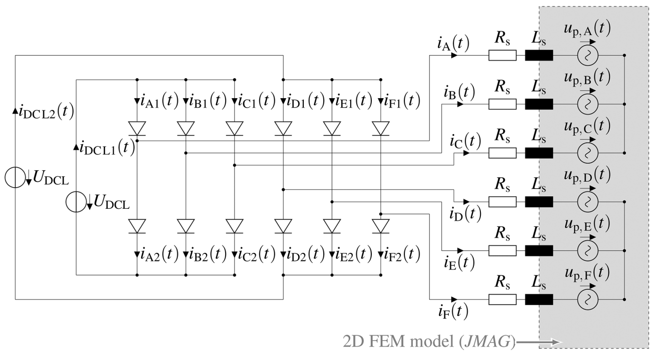

FIGURE 4 Schematic of the circuit for diode rectifier stator feeding, which is covered by the coupled numerical models. The three-phase subsystems with phases A, B, C and phases D, E, F feature separate neutral points and either common or separate DC links. Transient time stepping 2D FEM models in the software *JMAG* are used for the coupled analyses.

TABLE 2 Main geometry parameters of the HTS excited medium-speed generators. The large magnetic air gap width δ_{mag} includes the mechanical air gap, the damper, the cryostat wall and the vacuum spacing for thermal insulation, Figure 3 (a).

Active iron length	l_{Fe}	0.311 m
Stator outer radius	$d_{\mathrm{so}}/2$	0.933 m
Stator inner radius	r_{si}	0.815 m
Magn. air gap width	δ_{mag}	32.2 mm
Pole width / pole pitch	$w_{\mathrm{p}}/\tau_{\mathrm{pr}}$	0.425
Slot width / slot pitch	$s_{\mathrm{Q}}/\tau_{\mathrm{Qs}}$	0.513
Thickness cryostat wall	d_{vac}	5 mm
Thickness damper screen	d_{damp}	5 mm
Active generator mass	m_{act}	3.4 t

Each of the subsystems A, B, C and D, E, F is connected to a separate B6U rectifier with separate or common DC link. The connection of the subsystems in parallel ensures a low-voltage layout in the entire grid connection. The HTS field current $I_{\mathrm{f}}(n)$ is variable and adjusted to yield the required electrical output power $P_{\mathrm{el}}(n)$, Figure 2. The HTS field winding is designed for the most critical conditions at lowest speed $n_{\min} = 192\,\mathrm{rpm}$, that is, $\approx 38\%$ of rated speed, Figure 2 (d). The iterative design procedure is described in Section 3. Selected geometry parameters of the generator are listed in Table 2.

TABLE 3 Parameters of the copper stator winding in open slots. $L_{s,\sigma,b}$ is listed for rated operating conditions.

Phase count	m	6
Slots per pole per phase	q	1
Coil width / pole pitch	W/τ_{ps}	5/6
Copper slot fill factor	k_{Cu}	0.5
Turns per phase	N_s	15
Turns per coil	N_c	15
Parallel branches / phase	a	12
Rated current density	$J_{Cu,N}$	8.75 A/mm[3]
Rated current loading	A_{sN}	1470 A/cm
End-winding inductance	$L_{s,\sigma,b}$	14.6 µH
Stator phase resistance	R_s, 100°C	4.01 mΩ

TABLE 4 Parameters of the HTS field winding, made from *Fujikura FESC* EuBCO tape[13] with APCs (artificial pinning centers).

Tape width	w_t	12 mm
HTS temperature	T_{HTS}	30 K
Number of layers	n_{Lf}	2 (double racetrack)
Turns per pole	$N_{f,pol}$	2.75
Total tape length	l_{HTS}	3.75 km
Current margin	I_c/I_f	1.3
Critical current at 77 K, s.f.	I_{c0}	464 A

The six-phase copper stator winding features $a = 12$ parallel branches in order to keep the limits for state-of-the-art low-voltage windings, Table 3. The very high thermal utilization of the generator is enabled by a powerful cooling system, for example, indirect oil cooling, which is mandatory to exploit the advantages of a superconducting excitation.[12] The end-winding stray inductance is calculated from a comparison of 3D and 2D models, Section 3.

Since the operation with $\cos\varphi_s = -1$ at fixed stator voltage U_{sN} at n_{min} yields a very high excitation requirement per pole $\theta_{f,p} = n_{Lf} \cdot N_f \cdot I_f$, a wide HTS tape with $w_t = 12\,\text{mm}$ is chosen, Table 4. The EuBCO tape *FESC* with artificial pinning centers (APCs), made by *Fujikura*,[13] is used. The APCs prove beneficial under the high-field conditions at minimum speed $n_{min} = 192\,\text{rpm}$. The dependence of the critical current I_c on the local magnetic flux density $\vec{B}$ is incorporated, Sec. 3. A modified *Kim*-model with the lift factor (2) is used,[14] where the parameters k_s, B_0 and α_s are determined by fits to material data. For the design of the field winding, the worst local conditions, that is, with the lowest value of the critical current density $J_{c,min}\left(\vec{B}\right)$, in the HTS winding window are determined for each simulation run and the field current is adjusted to stay within the local limit $J_{c,min}/J_f = 1.3$. A liquid neon cooling at fixed cryogenic operating temperature $T = 30\,\text{K}$ is considered.

$$L\left(\vec{B}\right) = \frac{J_c\left(\vec{B}\right)}{J_c(B=0)} = \frac{1}{\left(1 + \frac{\sqrt{\left(k_s B_{\parallel}\right)^2 + B_{\perp}^2}}{B_0}\right)^{\alpha_s}} \tag{2}$$

3 | NUMERICAL MODELING FRAMEWORK

The numerical calculation scheme starts with an iterative design process of the field winding for the operating point $n_{min} = 192\,\text{rpm}$, $P_{el} = -0.25\,\text{MW}$, $U_{LL} = U_N = 690\,\text{V}$, $\cos\varphi_s = -1$. As the eddy current reaction field is of minor importance at this stage, a series of 2D non-linear magnetostatic FE-simulations with successively shifted rotor is used, Figure 5. Sinusoidal stator currents are impressed by means of source terms in the A-formulation. At the end of the

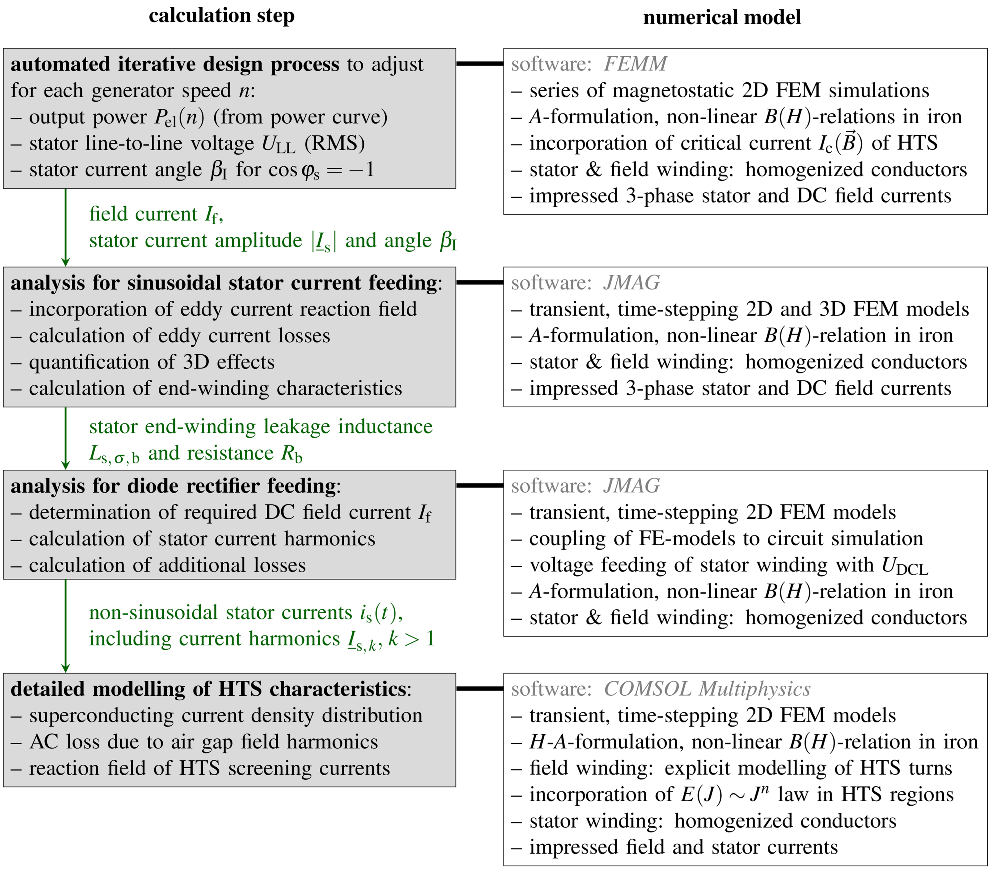

FIGURE 5 Schematic of the applied numerical calculation procedure for the analysis of the HTS medium-speed generator with diode rectifier stator feeding. Different software packages are selected for different models based on their computational efficiency and flexibility.

iterative procedure, which is implemented in *MATLAB*, the maximum superconducting field current $I_{\mathrm{f,max}}$ and the HTS winding's number of turns per pole $N_{\mathrm{f,pol}}$ are fixed. Based on this field winding design, a similar iterative procedure is used to determine the required field current $I_{\mathrm{f}}(n)$ for each of the operating points in the speed range $n_{\mathrm{min}}...n_{\mathrm{N}}$, Figure 2a.

Based on the preliminary field winding design and the excitation requirement $I_{\mathrm{f}}(n)$, transient, time-stepping 2D and 3D FE-models are implemented in *JMAG*[15] (*A*-formulation), Figure 5. Again, sinusoidal stator currents are impressed. The 2D FE-models provide the eddy current loss in the damper screen and in the cryostat wall and serve as reference for comparisons with the diode rectifier feeding. Moreover, the comparison of the 2D FE-models with results from 3D FE-models (Figure 6, *JMAG*) yield an accurate estimate (3) of the end-winding stray inductance $L_{\mathrm{s},\sigma,\mathrm{b}}$, Figure 3, with $\Psi_{\mathrm{s,3D}}$ and $\Psi_{\mathrm{s,2D}}$ as calculated stator flux linkages in the 3D and 2D FEM models, respectively. For this purpose, the end-winding section of the distributed stator winding is explicitly modeled, Figure 6. A parametric model of the end-winding together with a genetic algorithm are used to minimize the end-winding length l_{b}. $L_{\mathrm{s},\sigma,\mathrm{b}}$ features a non-linear dependence on the saturation state, so that calculations based on (3) are carried out for each excitation state $I_{\mathrm{f}} = 0...I_{\mathrm{f,max}}$, Figure 6.

$$L_{\mathrm{s},\sigma,\mathrm{b}} = \frac{\Psi_{\mathrm{s,3D}} - \Psi_{\mathrm{s,2D}}}{\sqrt{2} \cdot I_{\mathrm{s}}} \tag{3}$$

In the next step, transient 2D FE-models are coupled in *JMAG* to a circuit simulation, Figure 4, for a direct incorporation of the stator phase currents' non-sinusoidal time evolution $i_{\mathrm{s}}(t)$, details in Section 4. From these voltage-fed models, the additional eddy current loss in the normal-conducting damper and the cryostat wall as well as the additional stator iron loss due to stator current harmonics are calculated. A manually designed FE-mesh with $N_{\mathrm{e}} \approx 3 \cdot 10^4$

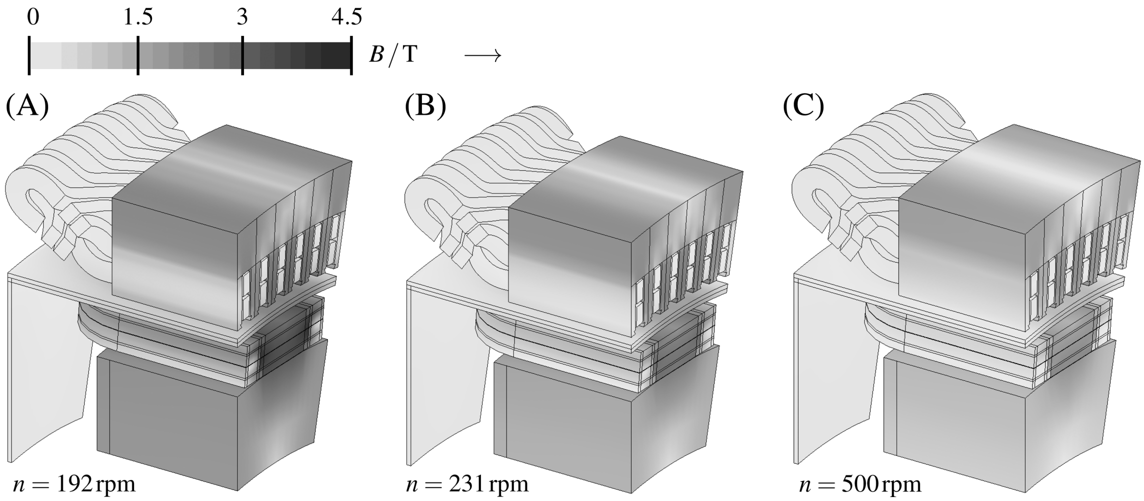

FIGURE 6 Numerically (FE-models) calculated flux density in one axial half of one pole (software: *JMAG*). Results are shown for a diode rectifier stator feeding with unity power factor $\cos\varphi_s = -1$ and fixed DC link voltage $U_{DCL} \approx 932\,\mathrm{V}$: (A) Minimum speed $n_{min} = 192\,\mathrm{rpm}$ with maximum field current $I_{f,max} = 1187\,\mathrm{A}$, (B) $n = 231\,\mathrm{rpm}$ with $I_f = 678\,\mathrm{A}$, (C) rated speed $n_N = 500\,\mathrm{rpm}$ with $I_{fN} = 193\,\mathrm{A}$. The flux density in the end-winding section is lower than in the straight active region, such that the design of the HTS field winding by means of 2D models, Figure 5, is reasonable. The stator leakage inductance $L_{s,\sigma,b}$ is determined from the difference between 3D and 2D FEM models, (3).

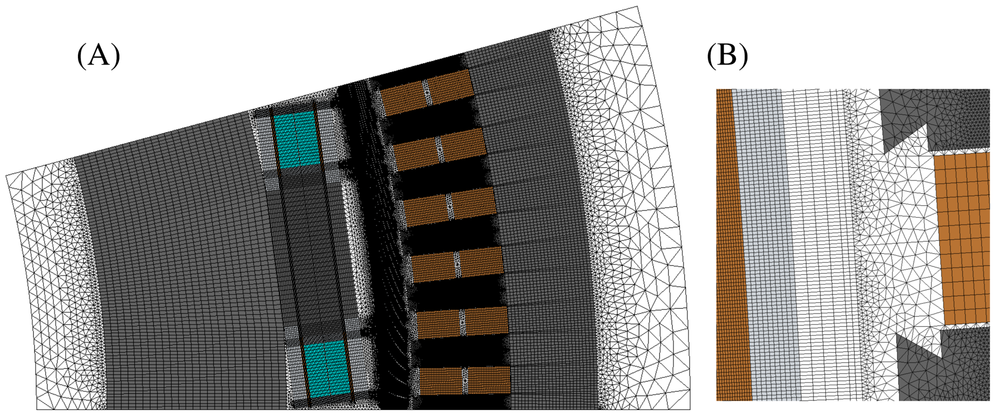

FIGURE 7 (A) Mesh in the 2D FE sector model, which is coupled to the circuit simulation, Figure 4. A manual meshing procedure is applied in the software *JMAG* via the *Python* interface in order reduce degrees of freedom while ensuring sufficient spatial resolution. (B) Detailed view of the air gap mesh and the slot opening.

first-order nodal elements per generator pole is used, Figure 7. The calculated eddy current loss in the vacuum chamber and the damper screen, as well as the calculated stator current harmonics $I_k, k > 1$ are prone to erroneous results in case of a too coarse meshing. All *JMAG* models feature homogenized conductor models for the copper stator winding and the HTS field winding. After equilibration to steady state conditions, the steady state stator phase currents $i_{s,j}(t), j \in \{A,B,C,D,E,F\}$ are extracted.

In a last step, the non-sinusoidal currents are impressed in current-fed 2D FEM models in the surface coupled *H-A*-formulation by means of source terms. The models are implemented in *COMSOL Multiphysics*[16] (details in Section 5) with detailed HTS coil models in order to calculate the superconducting current distribution and the hysteresis loss in the HTS winding. The combination of (i) surface coupled FE-models with $E(J)$-power law in the superconducting region and (ii) a coupling to the rectifier circuit with non-linear diode characteristic yields models with very poor convergence behavior, so that very small time steps and very long computation times are required. For this reason, the described two step procedure, Figure 5, is applied in favor of a separation of these strong non-linearities.

Three different software tools are used for their respective advantages at different calculation stages: *FEMM*[17] is very fast for magnetostatic 2D FEM calculations and provides convenient *MATLAB* and *Python* interfaces. These are required for the iterative design procedure, which is coordinated by means of an object-oriented *Python* framework. *JMAG* is optimized for fast transient, time stepping 2D and 3D simulations of electrical machines. It provides also a *Python* interface, which is used for the automated modeling and the creation of an efficient, customized mesh in the 3D model. Similar to *FEMM*, *JMAG* always uses an A-formulation for 2D models and does not allow for the coupling of different formulations. Therefore, *COMSOL Multiphysics* is used in the last step to meet this modeling requirement.

4 | COUPLED SIMULATION OF 2D FEM MODELS AND RECTIFIER CIRCUIT

The resistance characteristic of the diodes in Figure 4 is modeled with (4). In order to improve the convergence of the coupled simulation, lower and upper limits of the diode resistance $R_{\mathrm{D,max}} = 10^5\,\Omega$ and $R_{\mathrm{D,min}} = 10^{-5}\,\Omega$ are introduced without affecting the simulation results. The diode's $u_{\mathrm{D}}(i_{\mathrm{D}})$-relation introduces an additional non-linearity, Figure 8a, which requires small simulation time steps Δt. The coupled model does not convergence, if a too coarse mesh in the 2D FEM model is used, particularly in the iron regions with non-linear $B(H)$.

$$u_{\mathrm{D}}(t) = a \cdot \ln\left(\frac{I_{\mathrm{s}} + i_{\mathrm{D}}(t)}{I_{\mathrm{s}}}\right), \quad a = 0.026\,\mathrm{V},\, I_{\mathrm{s}} = 10^{-7}\,\mathrm{A} \tag{4}$$

Generally, the damper screen, the cryostat wall and the massive, electrically conductive rotor iron introduce time constants, with which transient eddy currents decay after the initial switch-on of the impressed currents. The equilibration to steady state conditions is therefore time-consuming and requires the use of successively reduced time steps Δt. Eddy currents in the rotor parts manifest also in a transient build-up of the electromagnetic torque $m_{\mathrm{e}}(t)$, Figure 8b, which differs among the different simulated operating points $\{P_{\mathrm{el}}, n\}$. As a general finding, an equilibration over more than $T_{\mathrm{sim}}/T_{\mathrm{s}} \approx 20 \ldots 60$ electrical periods is required in order to attain the steady state.

In spite of the same fundamental power factor $\cos\varphi_{\mathrm{s,1}} = -1$, the required excitation MMF $\theta_{\mathrm{f}} \sim I_{\mathrm{f}}$ generally differs between the diode rectifier stator feeding and the sinusoidal current feeding, Figure 5. In order to match the power curve, $P_{\mathrm{el}}(n)$, Figure 2a, the HTS field current is varied in the range $I_{\mathrm{f}} \approx 0.75 \cdot I_{\mathrm{f,sin}} \ldots 1.25 \cdot I_{\mathrm{f,sin}}$, where $I_{\mathrm{f,sin}}$ denotes the adjusted field current for sinusoidal stator currents. Varying the field current I_{f} corresponds to a variation of the back-EMF U_{p}, which together with the fixed DC link voltage U_{DCL} determines the power fed into the DC link (5), Figure 4.

$$P_{\mathrm{el,DCL}} = \frac{U_{\mathrm{DCL}}}{T_{\mathrm{s}}} \cdot \int_{t=0}^{T_{\mathrm{s}}} \left(i_{\mathrm{DCL1}}(t) + i_{\mathrm{DCL2}}(t)\right) \mathrm{d}t \tag{5}$$

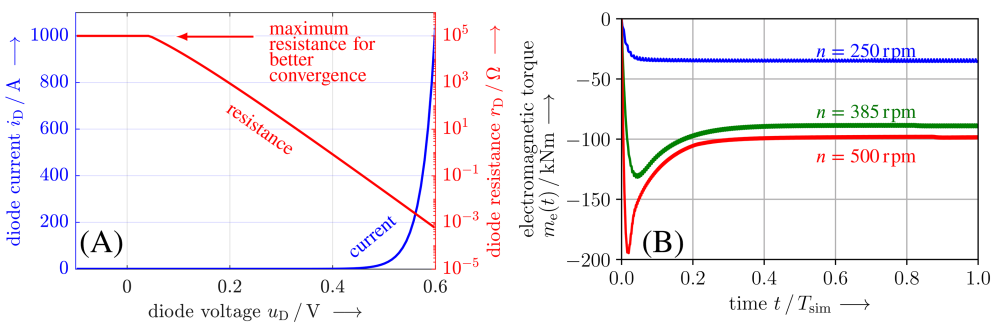

FIGURE 8 (A) Diode forward characteristic used for the coupled simulation, Figure 4, of the 2D FEM model and the diode rectifier model. (B) Numerically calculated electromagnetic torque for transient time-stepping simulations at different generator speeds n and excitations I_{f}. Very long settling times occur, which complicate the determination of the excitation requirement, Figure 9.

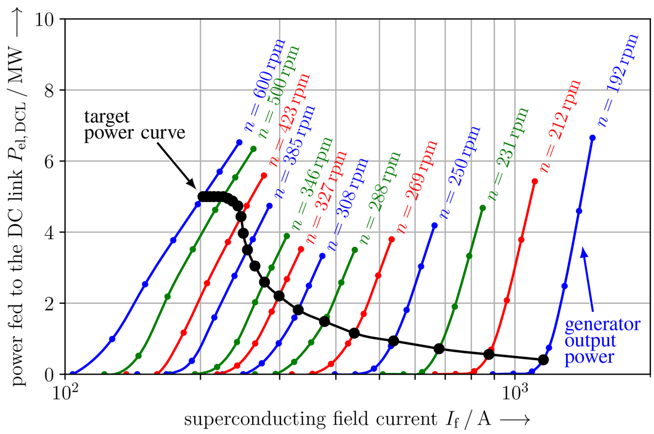

FIGURE 9 Numerical simulation results for passive diode rectifier stator feeding at constant DC link voltage $U_{DCL} \approx 932$V and different generator speeds n. For a given HTS field winding design (number of layers $n_{Lf} = 2$, number of turns per layer $N_{f,pol}/n_{Lf} = 75$), the field current I_f is varied in order to adjust the output power in accordance with the power curve in Figure 2 a). For $n > 350$ rpm, the $P_{el,DCL}(I_f)$-relations are shown only for selected speeds n for better visibility. The non-linear diode characteristic $i_D(u_D)$, Figure 8a, manifests in the abrupt increase of output power above a threshold voltage at the stator terminals.

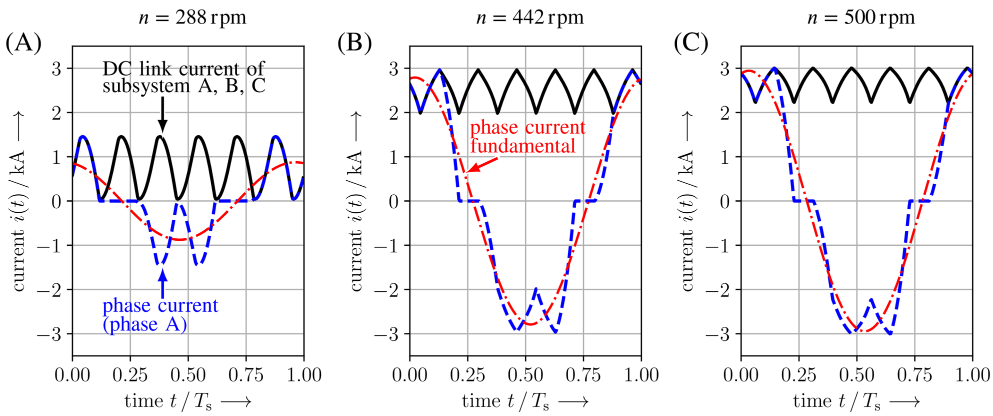

FIGURE 10 Numerically calculated DC link current i_{DCL} of the three-phase subsystem A, B, C, phase current $i_A(t)$ in phase A and its *Fourier* fundamental at diode rectifier feeding. The results are shown for (a) $n = 288$ rpm, $P_{el} \approx -1.48$ MW, $I_f \approx 352$ A, (b) $n = 442$ rpm, $P_{el} \approx -4.74$ MW, $I_f \approx 204$ A, (c) $n = 500$ rpm, $P_{el} = -5$ MW, $I_{fN} \approx 193$ A.

The non-linear diode characteristic, Figure 8a, manifests in an abrupt increase of generator output power $P_{el,DCL}$, Figure 9, as the HTS field current I_f is increased. A cubic interpolation is used to determine the required field current $I_{f,diode}(n)$, for which the generator performance is analyzed. As the generator-side passive diode rectifier replaces the usually employed IGBT rectifier, the superconducting field current I_f provides the only control degree of freedom for the power fed to the DC link. Therefore, field current variations are analyzed in Section 5.2.

The DC link current for one 3-phase subsystem A, B, C is shown in Figure 10 for exemplary generator speeds n and loads P_{el}. It features a pronounced ripple with $f/f_s = 6$ times electrical frequency. The current fed to the DC link by the subsystem D, E, F is shifted by $\omega_s t = 30^\circ$, such that the resulting current ripple in a common DC link is further reduced. If sufficiently small time steps are chosen to capture the sudden transition of the diodes from blocking to conducting, the simulation models converge reliably. The numerical stability of the FE-simulations can be further improved, if maximum relative deviations for the circuit variables, that is, the currents and voltages, are introduced as additional convergence criteria.

The peak value of the phase current $i_s(t)$ exceeds the fundamental amplitude $\widehat{I}_{A,k=1}$ in a wide range of generator speeds. The disadvantageous periodical interruption of the phase current, Figure 10, occurs also in the entire speed range, but is reduced as the generator load and, thus, the stator current increases, for example, at $n_N = 500$ rpm.

Prominent stator current harmonics with time orders $|k| = 5, 7, 11, 13$ occur in the three-phase subsystems. The harmonic RMS values for $|k| = 5$ and $|k| = 7$ feature maxima at partial load with $I_{k=5} \approx 460\,\mathrm{A}$ at $n \approx 350\,\mathrm{rpm}$ and $I_{k=7} \approx 250\,\mathrm{A}$ at $n \approx 290\,\mathrm{rpm}$. The harmonic RMS values I_k with time orders $|k| = 11, 13$ feature pronounced maxima at $n \approx 375\,\mathrm{rpm}$ with $I_{k=11} \approx 90\,\mathrm{A}$ and $I_{k=13} \approx 65\,\mathrm{A}$. At rated speed and load, the amplitudes are considerably smaller.

5 | SURFACE COUPLED MODELS OF THE HTS FIELD WINDING

The resistance characteristic of the HTS tapes is modeled with the power-law relation[14] (6), which reflects the finite resistance for $|J_z| < J_c$ due to flux creeping. The $\vec{B}$-dependent, local critical current density is calculated from (2) as $J_c\left(\vec{B}\right) = L\left(\vec{B}\right) \cdot J_c(B=0)$. A constant exponent of $n = 18$ is considered and the common value of the reference electrical field strength $E_c = 1\,\mu\mathrm{V/cm} = 10^{-4}\,\mathrm{V/m}$ is applied.[14]

$$E_z(J_z) = \frac{E_c}{J_c\left(\vec{B}\right)} \cdot \left(\frac{|J_z|}{J_c\left(\vec{B}\right)}\right)^{|n-1|} \cdot J_z, \quad \rho(J_z) = \frac{E_z(J_z)}{J_z} = \frac{E_c}{J_c\left(\vec{B}\right)} \cdot \left(\frac{|J_z|}{J_c\left(\vec{B}\right)}\right)^{|n-1|} \tag{6}$$

For the power law relation (6) the electrical conductivity $\kappa = 1/\varrho$ diverges for $|J_z| \to 0$, Figure 11b. As $\kappa(E_z)$ directly enters the equations for the A-formulation, (7), the convergence is problematic and the superconducting region cannot be modeled with the magnetic vector potential approach. Instead, the H-formulation is suitable, since only the resistivity $\rho(J_z)$ enters, which is finite for $J_z \to 0$. The H-formulation features however a worse convergence behavior for non-linear $B(H)$-relations in ferromagnetic domains.[18] Therefore, the coupled H-A-formulation[19] is applied, where the H-formulation part covers the HTS coil, Figure 12.

In the A-formulation domain, the equation to solve for the magnetic vector potential $\vec{A} = A_z \cdot \vec{e}_z$ is derived from *Ampère*'s law[22] as (7) with definitions of the magnetic flux density (8) and of the electric field strength (9). J_e denotes the externally impressed current density, for example, of the normal conducting stator field winding.

$$\kappa(E_z) \cdot \partial_t A_z - \partial_x(\nu(B) \cdot \partial_x A_z) - \partial_y\left(\nu(B) \cdot \partial_y A_z\right) = J_{e,z} \tag{7}$$

$$\vec{B} = \nabla \times \vec{A} = \partial_y A_z \cdot \vec{e}_x - \partial_x A_z \cdot \vec{e}_y \tag{8}$$

$$E_z = -\partial_t A_z \tag{9}$$

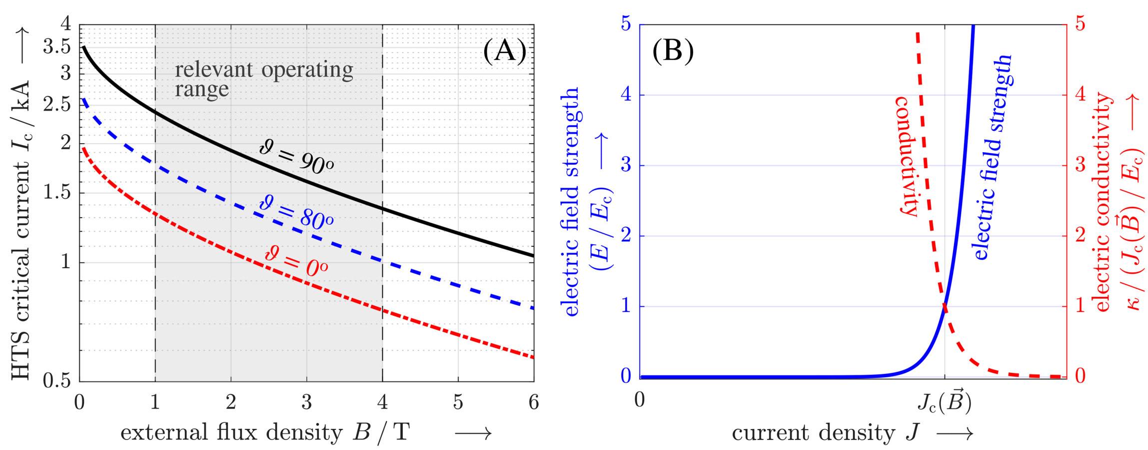

FIGURE 11 HTS tape: (A) Critical current I_c versus the absolute value of the external magnetic flux density B for different angles ϑ between $\vec{B}$ and the c-axis of the HTS layer. Considered tape: *Fujikura FESC*,[13] tape width: $w_t = 6\,\mathrm{mm}$. (B) Power law (6) with exponent $n = 18$ for the modeling of the $E(J)$-characteristic in the HTS winding. The non-linear electrical conductivity is shown as dashed line.

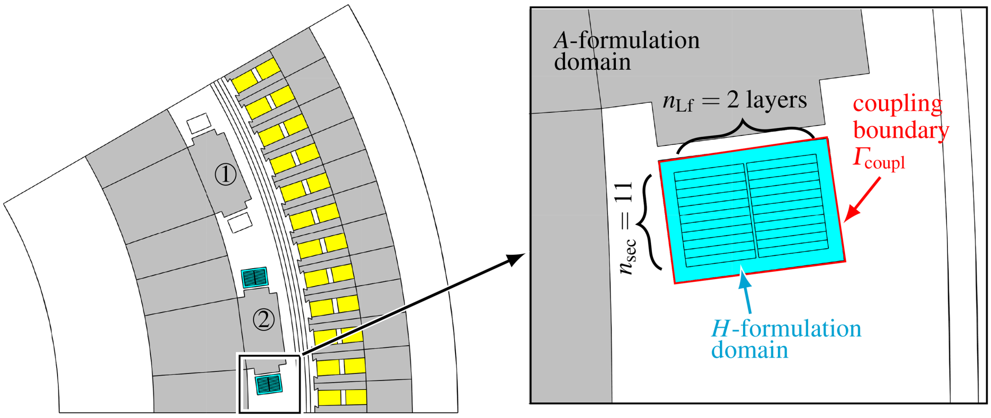

FIGURE 12 Two poles of the 2D FEM sector model of the six-phase medium-speed generator in the coupled *H*-*A*-formulation (software: *COMSOL Multiphysics*). The stator winding and the field winding of pole ① are modeled with homogeneous current densities J in the *A*-formulation part. The HTS coil of pole ② is modeled with homogenized individual turns[20,21] in the blue shaded *H*-formulation part to calculate the hysteresis loss and the superconducting current density distribution. The homogenized coil model with $n_{\mathrm{sec}} = 11$ explicitly modeled turns per layer is verified by comparison to a model, in which the actual number of turns $N_{\mathrm{f,pol}}/n_{\mathrm{Lf}} = 75$ per layer is modeled.

The *H*-formulation is based on *Faraday*'s law (10),[23] while the current density J_z is derived from $\nabla \times \vec{H} = \vec{J}$ as (11). The relation (12) in combination with (6) is not problematic in the superconducting region.[24]

$$\mu(H) \cdot \partial_t \vec{H} + \nabla \times \vec{E} = 0 \tag{10}$$

$$J_z = \partial_x H_y - \partial_y H_x \tag{11}$$

$$E_z = \rho(J_z) \cdot J_z \tag{12}$$

The coupling between the different domains at the coupling boundary contour Γ_{coupl}, Figure 12, is achieved by imposing weak contributions[19] (13) and (14). Here, $H_{\mathrm{t}} = \vec{H} \cdot \vec{t}$ denotes the magnetic field component, which is tangential to the coupling boundary ($\vec{t}$: tangential unit vector). ϑ_{A} is the scalar valued weighting function in the *A*-formulation part. The vector valued testing function in the *H*-formulation part is denoted by $\vec{\vartheta}_{\mathrm{H}}$, where $\vartheta_{\mathrm{H,t}} = \vec{\vartheta}_{\mathrm{H}} \cdot \vec{t}$ is its tangential component. First-order nodal elements are used in the *A*-formulation part, and first-order edge elements are used in the *H*-formulation part.

$$\int_{\Gamma_{\mathrm{coupl}}} H_{\mathrm{t}} \cdot \vartheta_{\mathrm{A}} \, \mathrm{d}\Gamma \quad \text{in } A\text{-formulation part (covering ferromagnetic generator parts)} \tag{13}$$

$$-\int_{\Gamma_{\mathrm{coupl}}} E_z \cdot \vartheta_{\mathrm{H,t}} \, \mathrm{d}\Gamma \quad \text{in } H\text{-formulation part (covering the superconducting field winding)} \tag{14}$$

For the HTS winding, only the HTS layer is modeled, as the hysteresis loss dominates the overall AC loss in the considered frequency range. A homogenized model[20] of the HTS field winding is used, where the actual number of $N_{\mathrm{f,pol}}/n_{\mathrm{Lf}} = 75$ turns per layer is replaced by $n_{\mathrm{sec}} = 11$ explicitly modeled regions per layer in the HTS winding window. Together with an artificial expansions[21] of the HTS layers' thickness, detail view in Figure 12, this leads to a significant reduction of the model's degrees of freedom. The simplified model is validated against a model with the actual number of $N_{\mathrm{f,pol}} = 2 \cdot 75$ regions featuring the actual HTS layer thickness $d_{\mathrm{HTS}} = 3\,\mu\mathrm{m}$.

After the initial ramp-up of the HTS field current, the transition to the steady state HTS current density profile $J_z\left(\vec{r}\right)$ occurs at very long time scales, which cannot be covered by time-stepping simulations. However, a steady state is much faster achieved, if the characteristic resistivity $\varrho_{\mathrm{c}} = E_{\mathrm{c}}/J_{\mathrm{c}}\left(\vec{B}\right)$ is artificially increased during a preliminary simulation run.

5.1 | HTS Hysteresis Loss Calculation at Stationary Operation

The hysteresis loss in the HTS field winding is calculated for rated load $P_{el} = -5\,\text{MW}$ at $n_N = 500\,\text{rpm}$, Figure 13a. This operation is regarded as the worst-case scenario in terms of hysteresis loss $P_{d,hyst}$ due to the highest stator current fundamental I_s, Figure 2a, and the highest stator frequency $f_s = 100\,\text{Hz}$. Still, the current margin I_c/I_f attains a maximum at rated conditions and the stator current harmonic amplitudes $I_k, k > 1$ are smaller than for intermediate generator speeds $n \approx 350...400\,\text{rpm}$, Figure 14. Therefore, artificially decreased current margins I_c/I_f, Figure 13b,c, are also considered in order to assess the general criticality of the additional hysteresis loss due to stator current harmonics. The hysteresis loss in the HTS regions is calculated from (21). Following main findings are obtained:

- At rated load, the calculated hysteresis loss $P_{d,hyst}$ is very small and in the same order of magnitude as for sinusoidal stator current feeding. Still, a pronounced oscillation of the instantaneous loss with $k = 12$ times electrical frequency

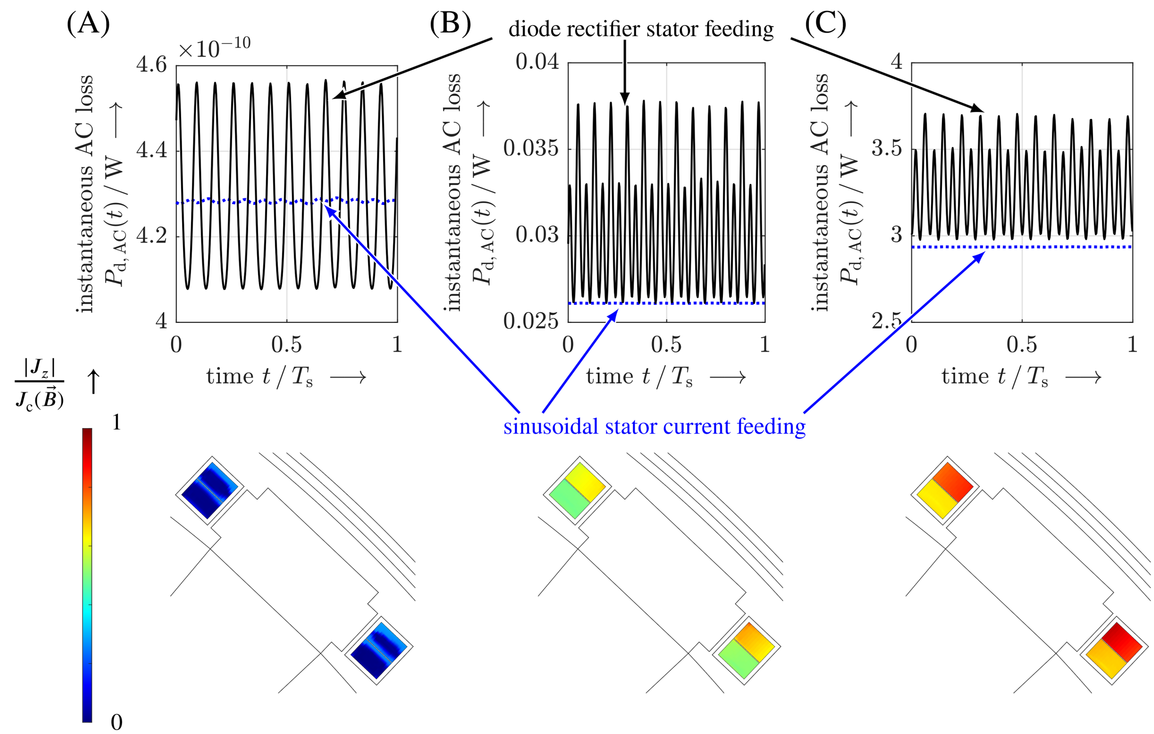

FIGURE 13 *Top*: Numerically calculated (*H-A*-formulation, software: *COMSOL Multiphysics*) instantaneous total hysteresis loss $P_{d,hyst}$ in the HTS field winding. The loss is shown for rated load at $n_N = 500\,\text{rpm}$, $P_{el,N} = -5\,\text{MW}$: (A) Current margin $I_c/I_f \approx 14$ in the original HTS field winding design for $\cos\varphi_s = -1$ at $n_{min} = 192\,\text{rpm}$, (B) current margin of $I_c/I_f \approx 1.7$, (C) current margin of $I_c/I_f \approx 1$. The hysteresis loss for sinusoidal current feeding is shown in blue, the results for passive diode rectifier feeding in black. *Bottom*: Numerically calculated ratio of the superconducting current density J_z and the field-dependent, local critical current density $J_c\left(\vec{B}\right)$ for the cases a–c.

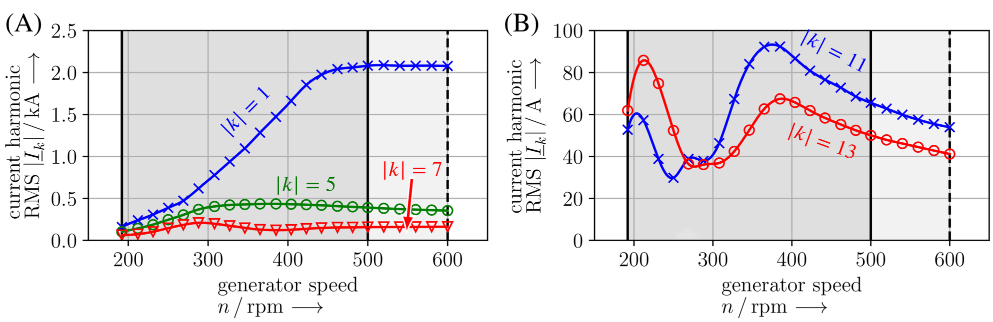

FIGURE 14 Numerically calculated (software: *JMAG*) RMS values of prominent stator phase current harmonics $|\widehat{\underline{I}}_k|$ at passive diode rectifier feeding in the entire speed and power range. (A) $|k| = 1, 5, 7$, (B) $|k| = 11, 13$.

f_s occurs, which is caused by stator current harmonics with time orders $|k| = 11, 13$. The very low hysteresis loss is attributed to the very high current margin $J_c(\vec{B})/|J_z| > 10$ in the entire HTS coil. For comparison, the simulations are also carried out for sinusoidal stator currents, which are impressed as source terms in the A-formulation part of the surface coupled models.

- For lower maximum current margins of $J_c(\vec{B})/|J_z| \approx 1.7$ and $J_c(\vec{B})/|J_z| \approx 1$ in the HTS winding, the hysteresis loss $P_{d,hyst}$ increases by orders of magnitude. However, $P_{d,hyst}$ is still very low and reaches only for $J_c(\vec{B})/|J_z| \approx 1$ about $P_{d,hyst} \approx 3\,W$. This is still small compared to the total heat load of the cryogenic cooling system in the order of $\dot{Q}_{cryo} \approx 30\,W$.
- As a general finding, the hysteresis loss in the DC HTS field winding $P_{d,hyst}$ due to stator current harmonics at diode rectifier feeding does not disqualify this alternative stator feeding concept.

5.2 | Variation of the Superconducting Field Current

As the superconducting field current I_f offers the only control degree of freedom for adjustments of the generator output power P_{el}, variations of the field current must be considered with respect to following requirements:

1. The hysteresis loss in the HTS winding at varying field current $i_f(t)$ must be sufficiently low.
2. The voltage requirement in the field circuit u_f must be determined, depending on the dynamical requirements, that is, the required slopes $di_f(t)/dt$.

The time scales, at which the field current i_f must be varied, generally depends on the required output power ramps, which are affected by wind fluctuations and operating strategies. To prevent additional assumptions and to obtain general results, only power ramps from $i_f = 0$ to $i_f = I_{f,max} = 1187\,A$ with different slopes are considered as example in this work. The slopes are defined by the parameter r in terms of the maximum field current $I_{f,max}$, (15).

$$\frac{di_f}{dt} = \frac{r \cdot I_{f,max}}{1s}, \quad r \in \{0.01, 0.02, 0.275, 2.75\} \tag{15}$$

In order to determine the field voltage requirement (2.), it is necessary to determine not only the resistive voltage drop $u_{r,f}$ in the field winding, but also the induced voltage $u_{i,f}$. In standard 2D FE-models of electrical machines in A-formulation, the induced voltage is calculated from the flux linkage, which is directly related to the z-component of the magnetic vector potential A_z. This is not possible in the surface coupled formulation, since A_z is not defined in the H-formulation part covering the HTS field winding.

A simple approach to calculate the induced field strength $E_{i,z}$ in the entire FE-model consists in introducing an additional variable U_z, which is solved for. U_z is defined in the entire simulation domain, comprising the H-formulation and the A-formulation part, and corresponds also to the z-component of the magnetic vector potential. The boundary conditions as well as the source terms $J_{e,z}$ (A-formulation part) for A_z and U_z are identical. In contrast to the governing equation (7) for A_z, the eddy current densities are however already known and enter as source terms in (16). Here, J_z comprises also the superconducting current density in the H-formulation part. The additional variable U_z is easily introduced in the software *COMSOL Multiphysics*.

$$-\partial_x(\nu(B) \cdot \partial_x U_z) - \partial_y(\nu(B) \cdot \partial_y U_z) = J_z + J_{e,z} \tag{16}$$

The induced electrical field strength is then calculated from the potential U_z as (17).

$$E_{i,z} = -\partial_t U_z \tag{17}$$

The resistive voltage drop $u_{r,f}^n$ and the induced voltage $u_{i,f}^n$ in the n^{th} modeled HTS region $n = 1, \ldots, (2 \cdot 2 \cdot n_{sec})$, that is, two layers with two coil sides each per pole, are calculated from (18) and (19). Here, S_n denotes the cross sectional area of the respective HTS region and L is the axial generator length, Table 2. The end-winding section of the field

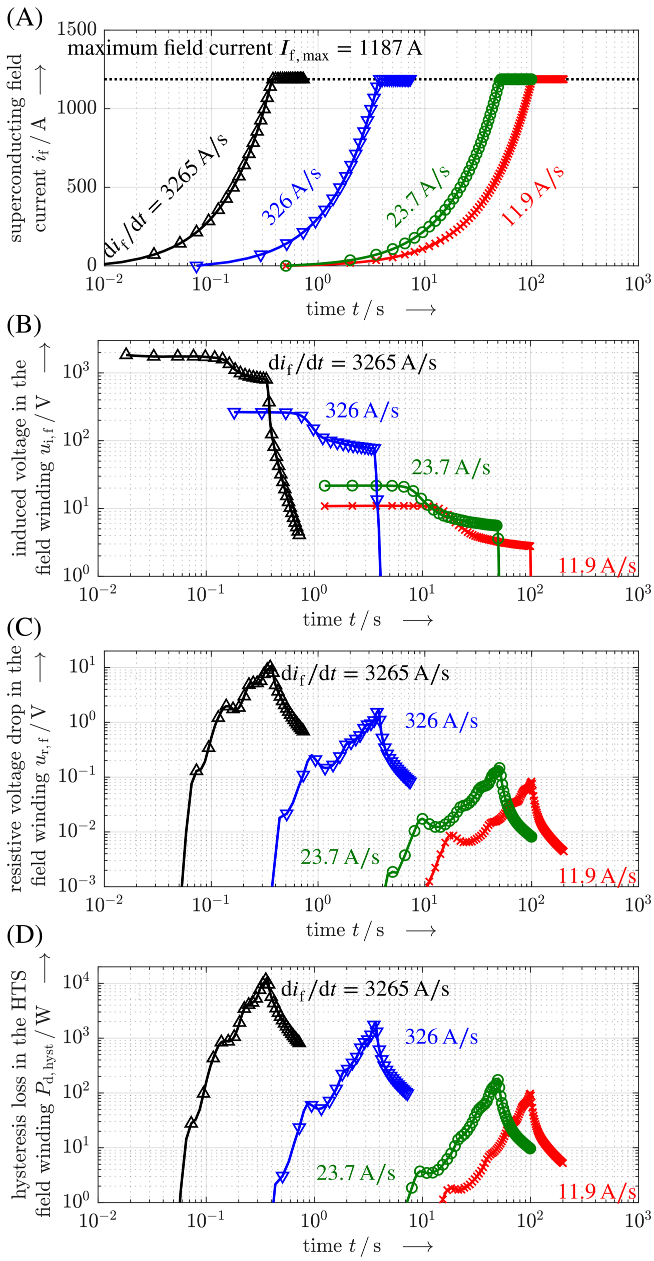

FIGURE 15 Numerically calculated results for HTS current ramps from $i_f = 0$ to maximum current $i_f = I_{f,max} = 1187$ A for four different slopes di_f/dt. (A) Field current in the HTS field winding, (B) induced voltage $u_{i,f}(t)$ in the series connection of all $2p = 24$ rotor poles, (C) as b) but for the resistive voltage drop $u_{r,f}(t)$, D) total instantaneous hysteresis loss in the entire HTS field winding $P_{d,hyst}(t)$. Models in the surface coupled *H-A*-formulation, implemented in *COMSOL Multiphysics*, are used.

winding is neglected, since it is short in the racetrack coil geometry. The electrical field strength E_z in (18) is obtained from (12) and covers only the resistive contribution according to (11).

$$u_{r,f}^n = L \cdot \frac{1}{S_n} \cdot \int_{S_n} E_z \mathrm{d}S \tag{18}$$

$$u_{i,f}^n = L \cdot \frac{1}{S_n} \cdot \int_{S_n} E_{i,z} \mathrm{d}S \tag{19}$$

The induced voltage $u_{i,f}$ in the series connection of all $2p = 24$ rotor poles is calculated from (20) by scaling to the actual number of winding turns $N_{f,pol}$.

$$u_{i,f} = 2p \cdot \frac{N_{f,pol}}{2 \cdot n_{sec}} \cdot \sum_{n=1}^{2 \cdot 2 \cdot n_{sec}} u_{i,f}^{n} \tag{20}$$

The total resistive voltage drop $u_{r,f}$ is calculated in a similar way. The hysteresis AC loss (21) is finally obtained by integrating the volumetric loss density $p_{d,hyst} = E_z \cdot J_z$ over the modeled HTS regions.

$$P_{d,hyst} = 2p \cdot L \cdot \sum_{n=1}^{2 \cdot 2 \cdot n_{sec}} \int_{S_n} (E_z \cdot J_z) \mathrm{d}S \tag{21}$$

The results for the four exemplary current slopes $\mathrm{d}i_f/\mathrm{d}t \in \{11.9\,\mathrm{A/s}, 23.7\,\mathrm{A/s}, 326\,\mathrm{A/s}, 3265\,\mathrm{A/s}\}$ are summarized in Figure 15. The considered current ramps start at $t = 0$ while the considered ramping time intervals cover 3 orders of magnitude, Figure 15a. The maximum current slope of $\mathrm{d}i_f/\mathrm{d}t > 3\,\mathrm{kA/s}$ must be regarded as extreme case, while current slopes of $\mathrm{d}i_f/\mathrm{d}t \approx 30\,\mathrm{A/s}$ correspond to typical maximum generator output power ramps of $0.6\,\mathrm{MW/min}$. Following main findings are obtained:

1. The induced voltage $u_{i,f}$, which must be compensated by the applied voltage u_f, decreases as the field current i_f increases, Figure 15b. This relation is caused by the decrease of the inductance L_f as the degree of iron saturation in the main flux path increases.
2. Even at a current slope of $\mathrm{d}i_f/\mathrm{d}t = 326\,\mathrm{A/s}$, the induced voltage does not exceed $u_{i,f} \leq 300\,\mathrm{V}$, Figure 15c. This implies sufficient dynamics at reasonable field voltage requirements.
3. The resistive voltage drop is generally small, that is, $u_{r,f} < 2\,\mathrm{V}$ for $\mathrm{d}i_f/\mathrm{d}t = 326\,\mathrm{A/s}$, and negligible compared to the induced voltage $u_{i,f}$. The maximum value of $u_{r,f}$ occurs at the end of the current ramp, when the lowest local current margins $J_c\left(\vec{B}\right)/|J_z|$ are reached. This corresponds to maximum instantaneous hysteresis losses $P_{d,hyst}$, Figure 15d.
4. The maximum instantaneous hysteresis loss in the HTS winding at moderate current slopes, that is, $\mathrm{d}i_f/\mathrm{d}t = 23.7\,\mathrm{A/s}$ and $\mathrm{d}i_f/\mathrm{d}t = 11.9\,\mathrm{A/s}$, is rather low and does not exceed $P_{d,hyst} \leq 200\,\mathrm{W}$. Compared to the cryogenic heat load estimate $\dot{Q}_{cryo} = 30\,\mathrm{W}$ at stationary operating conditions, i.e. constant I_f, this additional loss is manageable, if ramping events with high field current variation Δi_f are rare. In this regard, the ferromagnetic iron poles, Figure 3a, improve the thermal stability by providing a substantial heat capacity. More detailed analyses require a coupling to a thermal simulation, which is planned as future work.

6 | CONCLUSIONS

Six-phase medium-speed wind generators with high-temperature superconducting field winding are analyzed in the entire relevant operating range for diode rectifier feeding of the stator winding. The excitation requirements for unity power factor, speed-variable operation at fixed stator voltage is calculated by means of nonlinear FE-models. It is shown that the superconducting field winding can provide a sufficient excitation MMF, even at lowest generator speeds. This enables the cheap diode rectifier stator feeding in favor of reduced costs, higher efficiency and higher converter reliability. Coupled numerical models for the incorporation of stator current harmonics due to the diode rectifier are developed. Very long simulation settling times to reach steady state conditions and very fine meshes are identified as major challenges for the coupled models. The numerically calculated stator currents, including harmonics due to the diode rectification, are used to calculate the HTS hysteresis loss in the surface coupled *H-A*-formulation. As a second example, variations of the superconducting field current are analyzed. In both cases, the calculated hysteresis loss is low, thus recommending the diode rectifier stator feeding of HTS excited medium-speed generators as a promising alternative for future wind generator systems.

ACKNOWLEDGEMENTS

This work is supported by Stiftung Energieforschung Baden-Württemberg. Open Access funding enabled and organized by Projekt DEAL.

CONFLICT OF INTEREST STATEMENT

The authors declare no conflicts of interest.

DATA AVAILABILITY STATEMENT

The data that support the findings of this study are available from the corresponding author upon reasonable request.

ORCID

Robin Köster https://orcid.org/0000-0002-8806-8901

REFERENCES

1. Polinder H, Ferreira JA, Jensen BB, Abrahamsen AB, Atallah K, McMahon RA. Trends in Wind Turbine Generator Systems. *IEEE Trans Emerg*. 2013;1(3):174-185.
2. Haran KS, Kalsi S, Arndt T, et al. High power density superconducting rotating machines - development status and technology roadmap. *Supercond Sci Technol*. 2017;30(12):123002.
3. Bergen A et al. Design and in-field testing of the World's first ReBCO rotor for a 3.6 MW wind generator. *Supercond Sci Technol*. 2019; 32(125006):12.
4. Carrara S, Alves Dias P, Plazzotta B, Pavel C. Raw materials demand for wind and solar PV Technologies in the Transition Towards a decarbonised energy system. *Report of the Joint Research Centre (European Commission), no. EUR 30095 EN, Luxemburg*. 2020, pp. 11-15.
5. Hidding E, Jöckel A. *Giants of the Sea, the Next Ten Years*. Flender/Winergy Webcast, Flender Company; 2022.
6. Köster R, Binder A. "Medium-speed wind turbine generators with HTS excitation winding," in 2022 *International Conference on Electrical Machines* (*ICEM*), Valencia, Spain. 2022.
7. Köster R, Binder A. "Cost-oriented design considerations on direct-drive wind turbine generators with superconducting excitation winding," in *2021 International Aegean Conference on Electrical Machines and Power Electronics (ACEMP) & 2021 International Conference on Optimization of Electrical and Electronic Equipment (OPTIM)*, Brasov, Romania, 2021, 115-122.
8. Morgan EC, Lackner M, Vogel RM, Baise LG. Probability distributions for offshore wind speeds. *Energy Convers Manag*. 2011;52:15-26.
9. Vestas Wind Systems A/S. *V164-8.0 MW–Product Brochure*. Aarhus; 2011.
10. Song X, Buhrer C, Brutsaert P, et al. Designing and basic experimental validation of the World's first MW-class direct-drive superconducting wind turbine generator. *IEEE Trans Emerg*. 2019;34(4):2218-2225.
11. Voestalpine AG. *Data Sheet: Isovac 470-65A, Electrical Steel, Fully Processed*. Linz; 2018.
12. Gamble B, Snitchler G, MacDonald T. Full power test of a 36.5 MW HTS propulsion motor. *IEEE Transactions on Applied Superconductivity*. 2011;21(3):1083-1088.
13. Fujikura Ltd. Introduction of Fujikura RE-based HTS wire - product presentation. 2023 25 slides, Sakura, Japan.
14. Grilli F, Pardo E, Stenvall A, Nguyen DN, Yuan W, Gömöry F. Compu- tation of losses in HTS under the action of varying magnetic fields and currents. *IEEE Appl Supercond*. 2014;24(1):78-110.
15. JMAG® v. 23, www.jmag-international.com, JSOL, Tokyo, Japan.
16. COMSOL. Multiphysics® v. 6.2. www.comsol.com. COMSOL AB, Stockholm Sweden.
17. Meeker D. "Finite element method magnetics," Version 4.2. 2019 http://www.femm.info
18. Dular J, Harutyunyan M, Bortot L, Schöps S, Vanderheyden B, Geuzaine C. On the stability of mixed finite-element formulations for high-temperature superconductors. *IEEE Transactions on Applied Superconductivity*. 2021;31(6):8200412.
19. Brambilla R, Grilli F, Martini L, Bocchi M, Angeli G. A finite-element method framework for modeling rotating machines with superconducting windings. *IEEE Trans Appl Supercond*. 2018;28(5):5207511.
20. Liu D, Salmi T, Deng F, Ye C. Characteristics of the superconducting field winding of an HTS wind turbine generator during a short circuit fault. *IEEE Trans Appl Supercond*. 2022;32(4):5200606.
21. Ainslie M, Flack T, Campbell A. Calculating transport AC losses in stacks of high temperature superconductor coated conductors with magnetic substrates using FEM. *Physica C*. 2012;472:50-56.
22. Bíró O, Preis K. On the use of the magnetic vector potential in the fi nite- element analysis of three-dimensional eddy currents. *IEEE Transactions on Magnet-Ics*. 1989;25(4):3145-3159.
23. Bíró O. Edge element formulations of eddy current problems. *Comput Methods Appl Mech Eng*. 1999;169(3):391-405.

24. Zhang M, Yuan W, Kvitkovic J, Pamidi S. Total AC loss study of 2G HTS coils for fully HTS machine applications. *Supercond Sci Technol*. 2015;28:115011.

AUTHOR BIOGRAPHIES

Robin Köster M.Sc. Electrical Engineering, M.Sc. Industrial Engineering and M.Sc. Physics, Technical University Darmstadt in 2018, 2019 and 2020; Dr.-Ing. (PhD) degree for Electrical Engineering in 2023, Technical University Darmstadt; from 2019 to 2023 research assistant at the Institute of Electrical Energy Conversion, TU Darmstadt; since 2024 post-doctoral researcher at TU Darmstadt and research engineer at KSB, Frankenthal; field of research: electrical machines, superconductors in rotating electrical machines, wind power systems, pump drives, coupled multi-domain simulations.

Andreas Binder Senior Member IEEE, Member VDE, IET, VDI, EPE, received the degrees Dipl.-Ing. (diploma) and Dr. techn. (PhD) for Electrical Engineering from the University of Technology, Vienna/Austria, in 1981 and 1988, respectively. From 1981 to 1983 he worked at ELIN-Union AG, Vienna, on large synchronous generator design. From 1983 to 1989 he joined the Institute of Electrical Machines and Drives, Technical University, Vienna, as researcher. From 1989 to 1997 he rejoined industry, leading groups for developing DC and inverter-fed AC motors and drives, at Siemens AG, Bad Neustadt and Erlangen, Germany. Since 1994 he is lecturer (habilitation) at University of Technology, Vienna/Austria, and received in 1997 the ETG-Literature Award of the German Assoc. of Electrical Engineers, VDE. Since October 1997, he is Head of the Institute of Electrical Energy Conversion, Darmstadt University of Technology, as a full professor, being responsible for teaching and research for electrical machines, drives and railway systems. He is the author or co-author of more than 350 scientific publications and two books and holds several patents. He received Dr. h.c. from University of Technology Bucharest in 2007 and is the recipient of the Medal of Honor of the ETG/VDE 2009 for outstanding contributions at VDE. Research topics are High-Speed-Motors, Permanent magnet-E-Machines, bearing currents, drive technologies for hybrid and electric cars, drive systems for electric railways, magnetic suspension and magnetic bearings, generator systems.

How to cite this article: Köster R, Binder A. Numerical modeling of HTS excited medium-speed wind generators with diode rectifier stator feeding. *Int J Numer Model*. 2024;37(5):e3284. doi:10.1002/jnm.3284